

Topological transitions of spin-excitations in insulating chiral antiferromagnets

S. A. OWERRE¹

¹ *Perimeter Institute for Theoretical Physics - 31 Caroline St. N., Waterloo, Ontario N2L 2Y5, Canada*

PACS 75.10.Jm – Quantized spin models, including quantum spin frustration
PACS 73.43.-f – Quantum Hall Effects

Abstract – We present a comprehensive study of strain-induced topological magnon phase transitions in insulating three-dimensional (3D) topological chiral antiferromagnets on the kagome-lattice. We show that by applying (100) uniaxial strain, 3D insulating antiferromagnetic Weyl magnons (WMs) manifest as an intermediate phase between a strain-induced 3D magnon Chern insulator (MCI) with integer Chern numbers and a 3D trivial magnon insulator with zero Chern number. In addition, we show that strain suppresses the topological thermal Hall conductivity of magnons in these systems. Due to the similarity between 3D insulating and metallic kagome chiral antiferromagnets, we envision that the current results could also manifest in the 3D antiferromagnetic topological Weyl semimetals $\text{Mn}_3\text{Sn}/\text{Ge}$.

Introduction. – Three-dimensional (3D) topological semimetals are exotic phases of matter with gapless electronic excitations, which are protected by topology and symmetry. Their theoretical predictions and experimental discoveries have attracted considerable attention in condensed-matter physics [1–8]. They currently remain an active field of study. Nevertheless, the condensed matter realization of topological semimetals is essentially independent of the statistical nature of the quasiparticle excitations. In fact the notion of Weyl points was first observed experimentally in bosonic quasiparticle excitations [9].

There has been an intensive search for bosonic analogs of 3D topological semimetals in insulating quantum magnets with broken time-reversal symmetry [10–22]. Recently, topological Dirac magnons protected by a coexistence of inversion and time-reversal symmetry have been experimentally observed in a 3D collinear antiferromagnet Cu_3TeO_6 [14,15]. This has opened a great avenue for observing topological Weyl magnon (WM) points in 3D insulating quantum magnets. In magnetic bosonic systems, however, it is essentially important that the WM nodes occur at the lowest excitation if they were to make any significant contributions to observable thermal Hall transports. This is due to the population effect of bosonic quasiparticles at low temperatures. In this respect, WM nodes at the lowest excitation can be considered as the analog of elec-

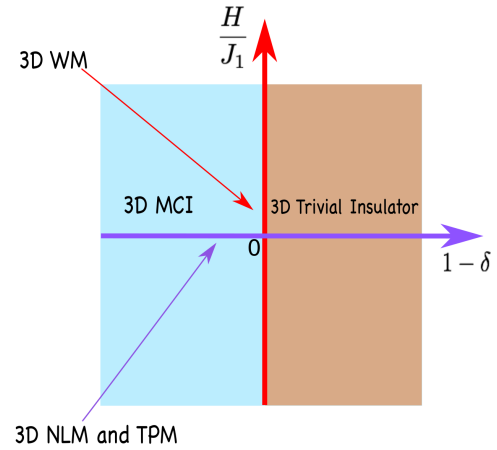


Fig. 1: Color online. Schematic of the topological magnon phase diagram studied in this paper. The horizontal axis represents the effect of uniaxial strain which we model as a change in the spin exchange coupling along the (100) direction. The vertical axis is the magnetic field along the (001) direction. There are four magnon phases in this system. The 3D NLM and 3D TPM appear at zero magnetic field or in the conventional non-collinear spin structure. The 3D WM phase appears in the unstrained limit at nonzero magnetic field in the non-coplanar spin structure. The two new magnon phases that appear due to strain in the noncoplanar spin structure are the 3D MCI and the 3D trivial insulator.

tronic Weyl points close to the Fermi energy. The WMs in the 3D kagome chiral antiferromagnet exhibit a topological thermal Hall effect [12]. Currently, they are the only known antiferromagnetic system in which the WM nodes occur at the lowest acoustic magnon branch and contribute significantly to the thermal Hall transports.

It is well-known that electronic ferromagnetic Weyl semimetal occurs as an intermediate phase between an ordinary insulator and a 3D quantum anomalous Hall insulator [2,23]. To our knowledge, this interesting topological phase boundary has not been established in 3D topological antiferromagnets. Thus far, the topological Dirac and Weyl nodes that appear in 3D insulating antiferromagnets [10–17] cannot transit to another topological magnon phase. In this respect, strain provides an effective way to tune the band structure of crystal in quantum materials. For instance, uniaxial strain can induce chiral anomaly and topological phase transitions in 3D topological Dirac and Weyl semimetals [24–31]. Moreover, strain can also induce a 3D topological Dirac semimetal in epitaxially-grown α -Sn films on InSb(111) [32]. We envision that such strain effects could be possible in 3D topological antiferromagnets.

In this letter, we propose a strain-induced topological magnon phase transition in 3D topological insulating chiral antiferromagnets. Due to the nature of the topological magnon band distributions in the 3D kagome chiral antiferromagnet, we have chosen this system for our study. However, our results can be extended to other 3D topological insulating antiferromagnets such as Cu_3TeO_6 [14,15]. We show that under (100) uniaxial strain, a topological magnon phase transition exist in the 3D topological insulating kagome chiral antiferromagnet.

We have identified four different magnon phases in this system as shown in Fig. (1). The 3D nodal-line magnon (NLM) and the triple point magnon (TPM) appear at zero magnetic field or at zero in-plane Dzyaloshinskii-Moriya interaction (DM) interaction [41,42] with a conventional 3D in-plane 120° non-collinear spin structure. They can be tuned by strain. The 3D WM phase appears in the unstrained limit at nonzero magnetic field or non-zero in-plane DM interaction with a noncoplanar chiral spin structure. The two new magnon phases that appear due to strained noncoplanar chiral spin structure are the fully gapped 3D MCI and the fully gapped 3D trivial insulator. We show that the former has integer Chern numbers, whereas the latter has zero Chern number. The study of the topological thermal Hall effect of magnons shows that the thermal Hall conductivity is suppressed in the fully gapped insulator phases. This implies that strain suppresses the thermal Hall conductivity of magnons.

Strained layered chiral antiferromagnets. – We study 3D kagome chiral antiferromagnets in the presence of (100) uniaxial strain and an external magnetic field along the (001) direction. The intralayer Heisenberg spin model in the presence of the DM interaction, interlayer

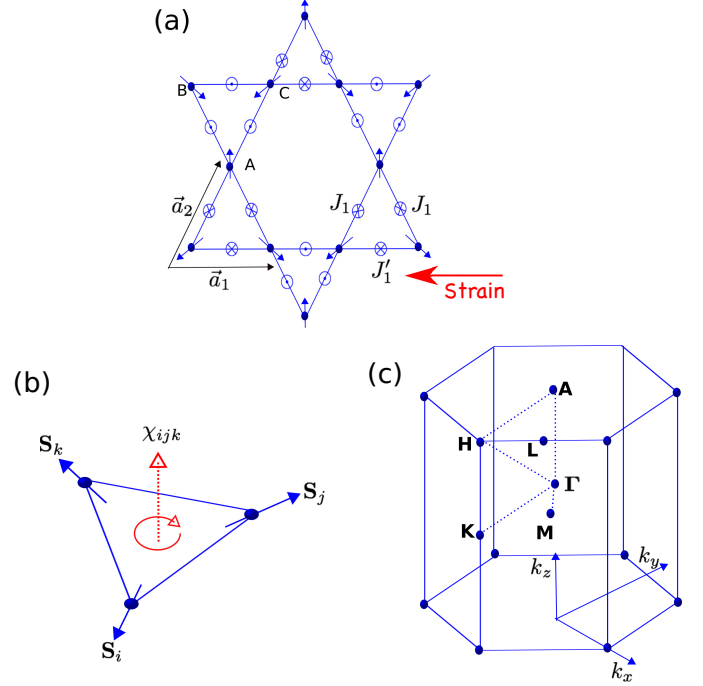


Fig. 2: Color online. (a) Top view of stacked kagome-lattice antiferromagnets along the (001) direction. The distribution of the DM interaction is denoted by the crossed and dotted circles. The blue arrows denote the conventional non-collinear spin order at zero magnetic field. A uniaxial strain is applied along the (100) direction. (b) Configuration of the scalar spin chirality on the kagome lattice. (c) The bulk Brillouin zone of the hexagonal lattices.

coupling, and an external magnetic field is given by

$$\mathcal{H} = \sum_{\langle ij \rangle, \ell} J_{ij} \vec{S}_i^\ell \cdot \vec{S}_j^\ell + \sum_{\langle ij \rangle, \ell} \vec{D}_{ij} \cdot \vec{S}_i^\ell \times \vec{S}_j^\ell + J_c \sum_{\langle \ell \ell' \rangle, i} \vec{S}_i^\ell \cdot \vec{S}_i^{\ell'} - \vec{H} \cdot \sum_{i, \ell} \vec{S}_i^\ell, \quad (1)$$

where \vec{S}_i^ℓ is the spin vector at site i in layer ℓ . The first term is the intralayer nearest-neighbour Heisenberg coupling. We model the effect of uniaxial strain along the (100) direction using the approximation that only the Heisenberg spin interaction along the in-plane x direction changes. In this case $J_{ij} = J_1$ along the diagonal bonds and $J_{ij} = J_1 \delta$ along the horizontal bonds, where δ is the strain as shown in Fig. 2(a). An alternative approximation is to consider isotropic Heisenberg interactions with lattice deformation in which only the primitive lattice vectors change. This will also modify the in-plane diagonal bonds, although to a lesser extent. We note that since the Weyl nodes in the isotropic limit is along the out-of-plane direction, it suffices to consider only the change along the in-plane horizontal bonds as the change along the in-plane diagonal bonds will not give any new topological phase transitions. In other words, the topological phase transition requires a modification of the in-plane

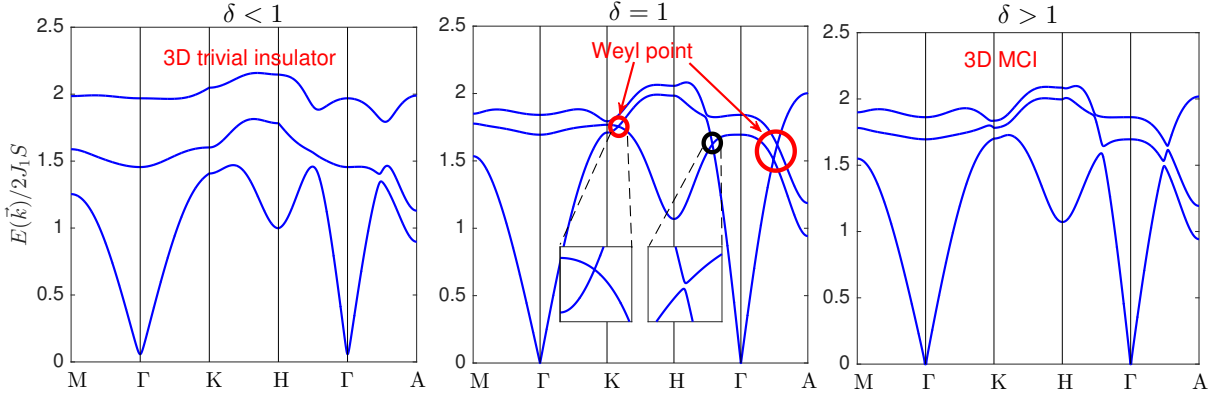


Fig. 3: Color online. Strain-induced topological magnon phase transitions in 3D kagome chiral antiferromagnets. (a) 3D trivial magnon insulator for $\delta = 0.75$, (b) 3D acoustic WM for $\delta = 1$, (c) 3D MCI for $\delta = 1.05$. The other parameters are set as $J_c/J_1 = 0.6$, $D/J_1 = 0.2$, $H/J_1 = 0.5$.

coupling constants. The second term is the out-of-plane ($\vec{D}_{ij} = \pm D\hat{z}$) DM interaction due to inversion symmetry breaking between two sites on each kagome layer. The DM interaction alternates between the triangular plaquettes of the kagome lattice and it stabilizes the conventional in-plane 120° non-collinear spin structure. Its sign determines the vector chirality of the non-collinear spin order [43]. The third term is the nearest-neighbour interlayer antiferromagnetic coupling between the kagome layers, which is inevitably present in real kagome materials [44–48]. Finally, the last term is an external magnetic field along the stacking direction $\vec{H} = g\mu_B H\hat{z}$, where g is the Landé g -factor and μ_B is the Bohr magneton.

In the absence of strain, *i.e.* $\delta = 1$, the 3D noncoplanar chiral kagome chiral antiferromagnets are intrinsic WM semimetals. The noncoplanar chiral spin texture with macroscopically broken time-reversal symmetry can be induced by an in-plane intrinsic DM interaction or an external magnetic field [12]. The WM phase in this system cannot transit to any other magnon phase by changing the parameters of the system at $\delta = 1$. Hence, it is strictly robust. In this paper, we will investigate the fate of the WM phase when a uniaxial strain is applied along the (100) direction. A similar effect can be induced by applying pressure. First, let us understand the spin structure at $H = 0$. In this case, the in-plane spins on each kagome layer are canted by the angle $\varphi = \arccos(-1/2\delta)$, where $\varphi \neq 120^\circ$ for $\delta \neq 1$. There are various magnetic phases for different limiting cases of δ . Nevertheless, our main concern here is the regime where the in-plane spins are non-collinear and stable. This happens in the regime $\delta > 1/2$.

Symmetry protection of in-plane noncollinear spin structure. — As previously discussed in ref. [12], the conventional 3D in-plane 120° spin structure at zero magnetic field preserves all the symmetries of the kagomé lattice. In particular, the combination of time-reversal symmetry (denoted by \mathcal{T}) and spin rotation denoted

by $\mathcal{R}_z(\pi)$ is a good symmetry [49], where $\mathcal{R}_z(\pi) = \text{diag}(-1, -1, 1)$ denotes a π spin rotation of the in-plane coplanar spins about the z -axis, and ‘diag’ denotes diagonal elements. In addition, the system also has three-fold rotation symmetry along the z direction denoted by \mathcal{C}_3 . The combination of mirror reflection symmetry $\mathcal{M}_{x,y}$ of the kagome plane about the x or y axis and \mathcal{T} (*i.e.* $\mathcal{T}\mathcal{M}_x\mathcal{T}$ or $\mathcal{M}_y\mathcal{T}$) is also a symmetry of the conventional in-plane 120° non-collinear spin structure [49, 57]. These symmetries are known as the “effective time-reversal symmetry” and they lead to nodal-line magnons and triply-degenerate nodal magnon points in the conventional 3D in-plane 120° spin structure of the stacked kagome antiferromagnets.

Field-induced noncoplanar chiral spin texture. —

Next, we induce noncoplanar chiral spin texture in the non-collinear regime by applying a magnetic field along the (001) stacking direction. We note that a noncoplanar chiral spin texture can also be induced if the intrinsic in-plane DM interaction is present [44–48]. Due to the presence of an out-of-plane DM interaction, a magnetically-ordered phase is present at low temperatures. In the ordered phase the magnetic excitations are magnons (quantized spin waves). They can be captured clearly in the linear spin wave theory approximation. First, let us express the spins in terms of local axes, such that the z -axis coincides with the spin direction. This can be done by performing a local rotation $\mathcal{R}_z(\theta_{i,\ell})$ about the z -axis by the spin orientated angles $\theta_{A,B,C} = 0, \varphi, -\varphi$, where $\varphi \neq 120^\circ$ for $\delta \neq 1$. As the external magnetic field induces canting of spins in the out-of-plane direction, we perform another rotation $\mathcal{R}_y(\chi)$ about y -axis by the angle χ . Now, the spins transform as

$$\vec{S}_{i,\ell} \rightarrow \mathcal{R}_z(\theta_{i,\ell}) \cdot \mathcal{R}_y(\chi) \cdot \vec{S}_{i,\ell}, \quad (2)$$

where the rotation matrices $\mathcal{R}_z(\theta_{i,\ell})$ and $\mathcal{R}_y(\chi)$ are given in the Supplemental Material (SM). Using the Holstein Primakoff transformation [50], the non-interacting spin-

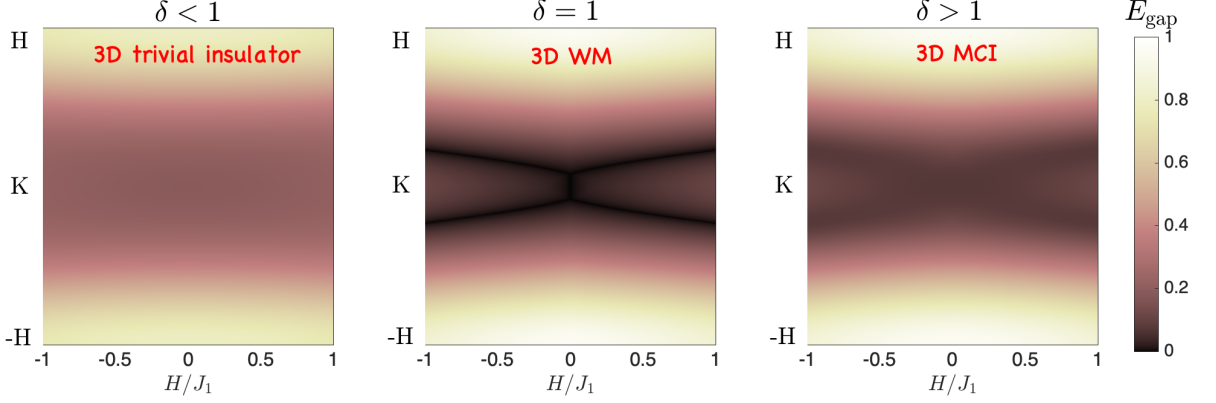


Fig. 4: Color online. Heat map of the energy gap between the two acoustic magnon branches as a function of the momentum along the high symmetry line $-H-K-H$ and magnetic field. (a) 3D trivial magnon insulator for $\delta = 0.75$. (b) 3D WMs for $\delta = 1$. (c) 3D MCI for $\delta = 1.05$. The other parameters are set as $J_c/J_1 = 0.6$, $D/J_1 = 0.2$.

wave Hamiltonian in momentum space can be written as

$$\mathcal{H} = S \sum_{\mathbf{k}, \alpha, \beta} 2 \left(\gamma_{\alpha\beta}^{(0)} \delta_{\alpha\beta} + \gamma_{\alpha\beta}^{(1)} \right) a_{\mathbf{k}\alpha}^\dagger a_{\mathbf{k}\beta} + \gamma_{\alpha\beta}^{(2)} \left(a_{\mathbf{k}\alpha}^\dagger a_{-\mathbf{k}\beta}^\dagger + a_{\mathbf{k}\alpha} a_{-\mathbf{k}\beta} \right), \quad (3)$$

where $\gamma_{\alpha\beta}^{(i)}$ are 3×3 matrices (see SM), and S is the value for the spin. The three sublattices on the kagome lattice are $\alpha, \beta = A, B, C$. Here, $a_{\mathbf{k}\alpha}^\dagger$ ($a_{\mathbf{k}\alpha}$) are the bosonic creation (annihilation) operators.

As shown in SM, a finite magnetic field $H \neq 0$ induces a noncoplanar chiral spin texture with finite scalar spin chirality [see Fig. 2(b)] given by

$$\chi_{ijk,\ell} = \cos \chi \vec{S}_{i,\ell} \cdot (\vec{S}_{j,\ell} \times \vec{S}_{k,\ell}), \quad (4)$$

where $\cos \chi = H/H_S(\delta)$ and the saturation field $H_S(\delta)$ is given in SM. In contrast to other magnetic Weyl systems that rely on time-reversal symmetry breaking by magnetic order, it is important to note that the scalar spin chirality breaks time-reversal symmetry macroscopically, and induces Weyl nodes at $\delta = 1$. At $H = 0$ the scalar spin chirality vanishes. In this case, the unstrained 3D kagome chiral antiferromagnet at $\delta = 1$ exhibits a coexistence of 3D NLM and 3D TPM due to the symmetry protection of the conventional 3D in-plane 120° spin structure at zero magnetic field as discussed above. These symmetry-protected nodal-line magnon phases can be tuned for $\delta \neq 1$ within the three magnon branches. Since an effective time-reversal symmetry is present at $H = 0$, there are no topological magnon phases in this system. At $H \neq 0$, however, a noncoplanar chiral spin texture with macroscopically broken time-reversal symmetry is induced. As we mentioned above, the magnon bands of unstrained 3D kagome chiral antiferromagnet at $\delta = 1$ possesses robust WM points in the noncoplanar regime, and they are the only topological magnon phase in this regime.

Strain-induced topological phase transitions. –

Remarkably, the strained 3D kagome chiral antiferro-

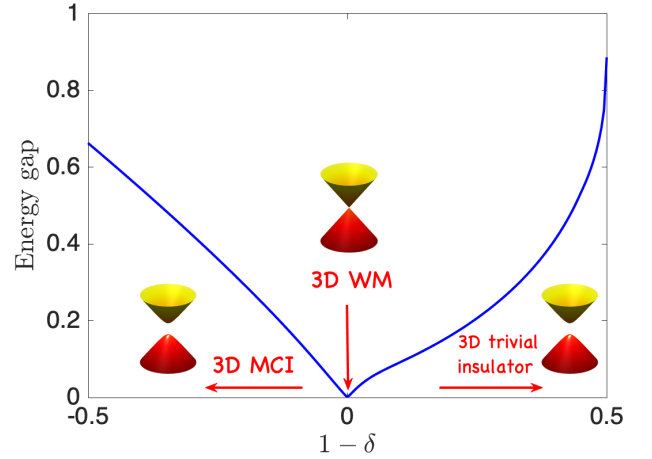


Fig. 5: Color online. Energy band gap between the two lowest acoustic magnon bands along $K-H$ high symmetry line as a function of strain. The parameters are $J_c/J_1 = 0.6$, $D/J_1 = 0.2$, and $H/J_1 = 0.5$.

magnet in the noncoplanar regime exhibits a topological magnon phase transition with interesting features. We will now investigate different aspects of these topological phase transitions. First, let us consider the 3D magnon band structures with varying δ . To establish a 3D spin structure, we fix a strong interlayer coupling $J_c/J_1 = 0.6$. In Fig. (3) we have shown the evolution of the 3D magnon bands along the Brillouin zone (BZ) paths in Fig. 2(c). We can see that the uniaxial strain along the (100) direction gaps out the 3D WM phase at $\delta = 1$ along the high symmetry lines $K-H$ and $\Gamma-A$ of the BZ. The Goldstone mode at the Γ point for $\delta \geq 1$ is due to broken continuous rotational symmetry about the z -axis, i.e. $U(\theta) = e^{i\theta S_z}$. The reason why there is no Goldstone mode in Fig. 3(a) is because the chosen $\delta = 0.75$ is close to the critical point $\delta = 0.5$ below which there is a change of magnetic order.

Let us define the gap between the two acoustic magnon

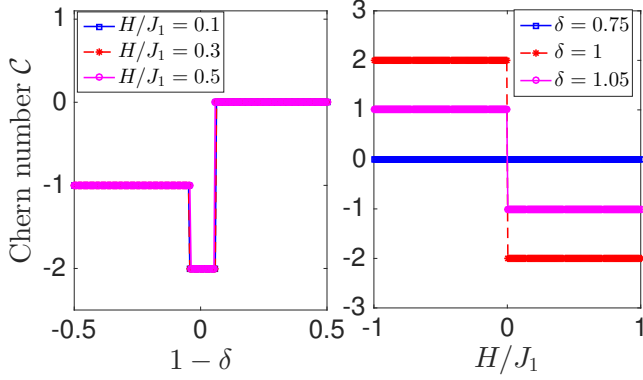


Fig. 6: Color online. (Left) Chern number of the lowest acoustic magnon band as a function of strain δ for different values of the magnetic field. (Right) Chern number of the lowest acoustic magnon band as a function of the magnetic field H/J_1 for different values of strain δ . The other parameters are set as $J_c/J_1 = 0.6$, $D/J_1 = 0.2$.

branches as $E_{gap} = 2|E_2(\mathbf{k}) - E_1(\mathbf{k})|$. At the WM points E_{gap} vanishes, and the fully gapped magnon insulators are characterized by a non-zero E_{gap} along the high symmetry lines of the BZ. Next, let us check if the regime $\delta \neq 1$ is truly a fully gapped magnon insulator with $E_{gap} \neq 0$ for varying magnetic field in the noncoplanar regime. For this purpose, we have fixed the antiferromagnetic interlayer coupling to $J_c/J_1 = 0.6$ and the DM interaction to $D/J_1 = 0.2$. We then plot the heat map of E_{gap} as a function of the momentum along the high symmetry lines and the magnetic field in the noncoplanar regime. The heat map of E_{gap} is shown in Figs. 4(a)–(c) for different regimes of δ . At the critical point $\delta = 1$ we can see that gapless points (black lines) appear between the two acoustic magnon branches, which signify the presence of WM points along $-H-K-H$ lines. In the regimes $\delta < 1$ and $\delta > 1$ there are no discernible gapless points along the $-H-K-H$ line of the BZ. Therefore these two regimes define fully gapped magnon insulators, however with different properties as we will see later. Furthermore, in Fig. (5) we have shown the evolution of the magnon energy band gap E_{gap} along the $K-H$ high symmetry line as a function of the strain parameter δ . We can see that the three distinct regions are clearly identified. We have checked that similar trends are manifested along the $-A-\Gamma-A$ line.

Now, we will consider the Chern number topological phase transition of the system. This will justify the topological and non-topological regimes of δ . We will focus on the lowest acoustic magnon branch in which the strain-induced topological phase transition occurs. In this case, we can formally define the 3D trivial magnon insulator as the state where the Chern number of the lowest acoustic magnon branch vanishes, and a 3D MCI as the state with non-zero integer Chern numbers. The 3D antiferromagnetic system can be considered as slices of 2D antiferromagnetic MCIs [52, 53] interpolating between the $k_z = 0$

and $k_z = \pi$ planes. For an arbitrary k_z point the Chern number of the magnon energy branches can be defined as

$$\mathcal{C}_n = \frac{1}{2\pi} \int_{BZ} d\mathbf{k}_{\parallel} \Omega_{xy}^n(\mathbf{k}_{\parallel}, k_z), \quad (5)$$

where $\mathbf{k}_{\parallel} = (k_x, k_y)$ is the in-plane momentum vector and $\Omega_{\alpha\beta}^n(\mathbf{k}_{\parallel}, k_z)$ is the momentum space Berry curvature for a given magnon band n as shown in SM.

For an arbitrary k_z point and $\delta \neq 1$ the Chern number is well-defined in the noncoplanar regime. The Chern number of all the 2D slices at an arbitrary k_z point is the same because the planes at two k_z points can be adiabatically connected without closing the gap for $\delta \neq 1$. For $\delta = 1$ the net contribution to the Chern number comes from the regime $-k_z^c < k_z < k_z^c$, where k_z^c is the location of the Weyl points along the k_z momentum direction. Based on this consideration, we have shown the plots of the Chern number of the lowest acoustic magnon band as a function of strain δ for different values of H/J_1 in Fig. 6(a), and as a function of the magnetic field H/J_1 for different values of δ in Fig. 6(b). In both figures, we can see that the regime $\delta < 1$ has zero Chern numbers. Therefore, the system is a 3D trivial magnon insulator for $\delta < 1$. For small magnetic field in the regime $\delta > 1$, however, the Chern number of lowest acoustic magnon band is $\mathcal{C} = -1$ and changes its sign as the sign of the magnetic field is flipped. At the 3D WM phase $\delta = 1$, the Chern number is $\mathcal{C} = -2$ for small magnetic field.

Topological thermal Hall effect. – Having identified the different magnon phases in the strained 3D kagome chiral antiferromagnet, we will now study an experimentally feasible measurement that can be performed on this system. The topological thermal Hall effect of magnons refers to the generation of a transverse thermal Hall voltage in the presence of a longitudinal temperature gradient due to the presence of noncoplanar chiral spin textures. In principle, it does not necessarily require the DM interaction provided a noncoplanar chiral spin configuration can be established, for example by adding further nearest-neighbour interactions. Therefore, the topological thermal Hall effect of magnons is different from the conventional magnon thermal Hall effect in insulating ferromagnets which strictly requires the DM interaction [33–40].

In the 3D model, the topological thermal Hall conductivity has three contributions κ_{yz}^{3D} , κ_{zx}^{3D} , and κ_{xy}^{3D} , where the components are given by [38]

$$\kappa_{\alpha\beta}^{3D} = -k_B T \int_{BZ} \frac{d\mathbf{k}}{(2\pi)^3} \sum_{n=1}^N c_2(f_n^B) \Omega_{\alpha\beta}^n(\mathbf{k}), \quad (6)$$

where $f_n^B = (e^{E_n(\mathbf{k})/k_B T} - 1)^{-1}$ is the Bose occupation function, k_B the Boltzmann constant which we will set to unity, T is the temperature and $c_2(x) = (1+x) (\ln \frac{1+x}{x})^2 - (\ln x)^2 - 2\text{Li}_2(-x)$, with $\text{Li}_2(x)$ being the dilogarithm. In Eq. (6), we have dropped the term $-\frac{\pi^2}{3} \sum_{n=1}^N \Omega_{\alpha\beta}^n(\mathbf{k})$,

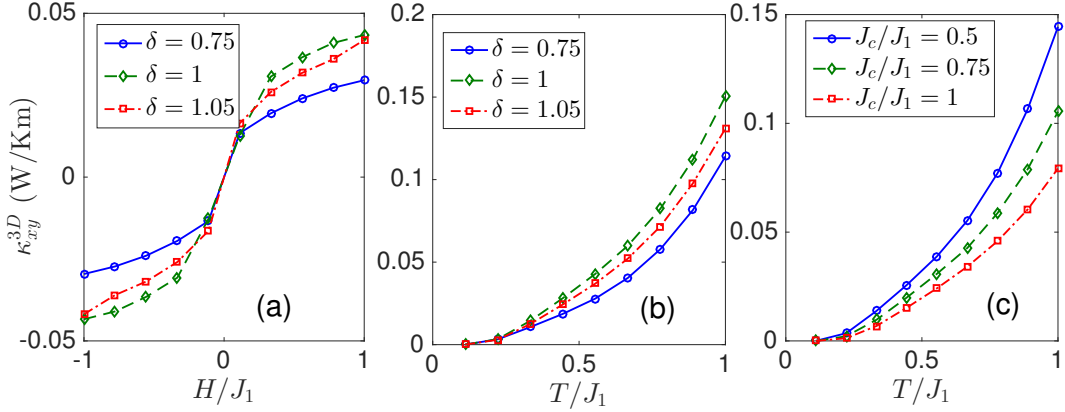


Fig. 7: Color online. (a) Plot of κ_{xy}^{3D} vs. H/J_1 for $T/J_1 = 0.5$, $J_c/J_1 = 0.6$, and different regimes of δ . (b) κ_{xy}^{3D} vs. T/J_1 for $H/J_1 = 0.5$, $J_c/J_1 = 0.6$, and different regimes of δ . (c) κ_{xy}^{3D} vs. T/J_1 for $H/J_1 = 0.5$, $\delta = 1.05$ and different values of J_c/J_1 . The DM interaction is $D/J_1 = 0.2$ for all figures.

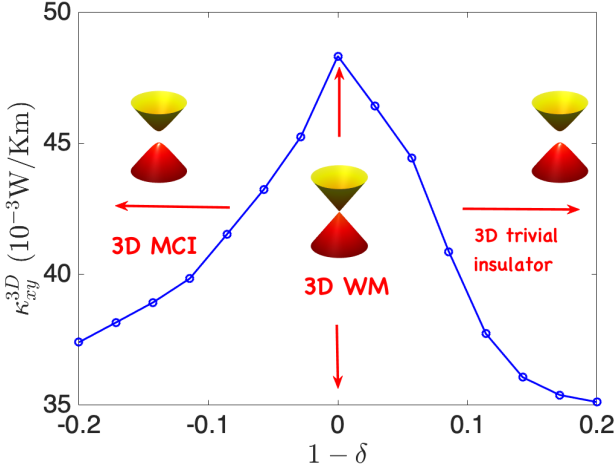


Fig. 8: Color online. Plot of κ_{xy}^{3D} vs. $1 - \delta$ for $T/J_1 = 0.35$, $J_c/J_1 = 0.6$, $D/J_1 = 0.2$, and $H/J_1 = 0.5$.

since the sum of the Berry curvature of the three magnon bands is zero.

Due to the Bose occupation function, the dominant contribution to $\kappa_{\alpha\beta}^{3D}$ comes from the lowest magnon branch, where the topological phase transitions occur in the current system. As the noncoplanar chiral spin configuration is induced along the z direction, the first two components κ_{yz}^{3D} and κ_{zx}^{3D} vanish. The only nonzero component is κ_{xy}^{3D} . In Figs. 7(a) and (b) we have shown the trends of κ_{xy}^{3D} as a function of the magnetic field and temperature respectively for different regimes of δ . We find that the magnitude of κ_{xy}^{3D} is suppressed in the 3D insulator phases. In other words, strain decreases the thermal Hall conductivity. We note that in the 3D WM phase the magnitude of κ_{xy}^{3D} is dominated by the states near the WM nodes at the lowest magnon branch due to large Berry curvatures. In this case the thermal Hall conductivity is proportional to the distance separating the WM nodes in momentum

space in analogy to the anomalous Hall conductivity in Weyl semimetals [2]. In the 3D insulator phases the magnitude of κ_{xy}^{3D} is dominated by the states near the topological gaps at the lowest magnon branch. Despite zero Chern number in the 3D trivial insulator phase, we can see that κ_{xy}^{3D} is nonzero for $\delta < 1$. This is in stark contrast to electronic systems where the Fermi energy can guarantee a completely filled band and zero Hall conductivity in the trivial insulator phase. In magnonic (bosonic) systems the Bose occupation function eliminates this restriction as the bands are thermally populated. Therefore, the thermal Hall effect in insulating quantum magnets is not a direct consequence of Chern number protected topological bands. It depends solely on the Berry curvature of the magnon bands irrespective of their topological classifications. In Fig. 7(c), we have shown the temperature dependence of κ_{xy}^{3D} for varying interlayer coupling in the MCI phase for $\delta = 1.05$. We can see that the increase in the interlayer coupling decreases κ_{xy}^{3D} . The plot of κ_{xy}^{3D} vs. $1 - \delta$ at low temperature $T/J_1 = 0.35$ depicted in Fig. 8 shows the three regimes in the topological phase diagram. Evidently, the thermal Hall conductivity of Weyl magnons is maximum because they carry the dominant contribution of the Berry curvature.

Conclusion. — We have proposed a strain-induced topological phase transitions in 3D topological insulating chiral antiferromagnets. We showed that in the presence of (100) uniaxial strain, the antiferromagnetic WM in 3D topological insulating antiferromagnets is an intermediate phase between a 3D antiferromagnetic MCI with integer Chern numbers and a 3D antiferromagnetic trivial insulator with zero Chern number. We further showed that the thermal Hall conductivity of magnons is suppressed in the 3D insulator phases. Besides, we found that the 3D trivial magnon insulator with zero Chern number possess a non-zero thermal Hall conductivity due to the bosonic nature of magnons. We believe that our results can be investigated experimentally in various 3D insulating anti-

ferromagnets by applying uniaxial strain or pressure. For the 3D kagome chiral antiferromagnets, there are various promising materials that have been synthesized lately [44–48]. Furthermore, it will be interesting to experimentally investigate the effects of strain on the recently observed 3D topological Dirac magnons in the insulating antiferromagnet Cu_3TeO_6 [14,15]. As previously mentioned, we envision that the current results could also manifest in the 3D antiferromagnetic topological Weyl semimetals $\text{Mn}_3\text{Sn}/\text{Ge}$ [54–59].

* * *

Research at Perimeter Institute is supported by the Government of Canada through Industry Canada and by the Province of Ontario through the Ministry of Research and Innovation.

REFERENCES

- [1] X. Wan, A. M. Turner, A. Vishwanath, and S. Y. Savrasov, *Phys. Rev. B* **83**, 205101 (2011).
- [2] A. A. Burkov and L. Balents, *Phys. Rev. Lett.* **107**, 127205 (2011).
- [3] Z. Wang, Y. Sun, X. -Q. Chen, C. Franchini, G. Xu, H. Weng, X. Dai, and Z. Fang, *Phys. Rev. B* **85**, 195320 (2012).
- [4] Z. K. Liu et al., *Science* **343**, 864 (2014).
- [5] S.-Y. Xu et al. *Science* **349**, 613 (2015).
- [6] B. Q. Lv, et al., *Phys. Rev. X* **5**, 031013 (2015).
- [7] P. Tang, Q. Zhou, G. Xu, and S.-C. Zhang, *Nat. Phys.* **12**, 1100 (2016).
- [8] N. P. Armitage, E. J. Mele, and A. Vishwanath. *Rev. Mod. Phys.* **90**, 015001 (2018).
- [9] L. Lu, Z. Wang, D. Ye, L. Ran, L. Fu, J. D. Joannopoulos, and M. Soljačić, *Science* **349**, 622 (2015).
- [10] F. -Y. Li, Y. -D. Li, Y. B. Kim, L. Balents, Y. Yu, G. Chen, *Nat. Commun.* **7**, 12691 (2016).
- [11] S. -K. Jian and W. Nie, *Phys. Rev. B* **97**, 115162 (2018).
- [12] S. A. Owerre, *Phys. Rev. B* **97**, 094412 (2018).
- [13] K. Li, C. Li, J. Hu, Y. Li, and C. Fang, *Phys. Rev. Lett.* **119**, 247202 (2017).
- [14] W. Yao, C. Li, L. Wang, S. Xue, Y. Dan, K. Iida, K. Kamazawa, K. Li, C. Fang, Y. Li, *Nature Physics* **14**, 1011 (2018).
- [15] S. Bao et al., *Nat. Commun.* **9**, 2591 (2018).
- [16] S. A. Owerre, *Europhys. Lett.* **120**, 57002 (2017).
- [17] K. Hwang, N. Trivedi, and M. Randeria. *arXiv:1712.08170*.
- [18] A. Mook, J. Henk, and I. Mertig, *Phys. Rev. Lett.* **117**, 157204 (2016).
- [19] Y. Su, X. Wang, X. S. and X. R. Wang, *Phys. Rev. B* **95**, 224403 (2017).
- [20] K. -K. Li and J.-P. Hu, and *Chin. Phys. Lett.* **34**, 077501 (2017).
- [21] Y. Su and X. R. Wang, *Phys. Rev. B* **96**, 104437 (2017).
- [22] V. A. Zyuzin, and A. A. Kovalev, *Phys. Rev. B* **97**, 174407 (2018).
- [23] Y. J. Jin, R. Wang, B. W. Xia, B. B. Zheng, and H. Xu, *Phys. Rev. B* **98**, 081101(R) (2018).
- [24] D. I. Pikulin, A. Chen, and M. Franz, *Phys. Rev. X* **6**, 041021 (2016).
- [25] D. Shao, J. Ruan, J. Wu, T. Chen, Z. Guo, H. Zhang, J. Sun, L. Sheng, and D. Xing, *Phys. Rev. B* **96**, 075112 (2017).
- [26] T. Nie, L. Meng, Y. Li, Y. Luan and J. Yu, *Phys.: Condens. Matter* **30** 125502 (2018).
- [27] A. Cortijo, Y. Ferreirós, K. Landsteiner, and M. A. H. Vozmediano *Phys. Rev. Lett.* **115**, 177202 (2015).
- [28] A. Cortijo, D. Kharzeev, K. Landsteiner, and M. A. H. Vozmediano *Phys. Rev. B* **94**, 241405(R) (2016).
- [29] A. G. Grushin, J. W. F. Venderbos, A. Vishwanath, and R. Ilan, *Phys. Rev. X* **6**, 041046 (2016).
- [30] J. Behrends, S. Roy, M. H. Kolodrubetz, J. H. Bardarson, A. G. Grushin, *arXiv:1807.06615*.
- [31] Y. Ferreiros, Y. Kedem, E. J. Bergholtz, J. H. Bardarson, *arXiv:1808.08241*.
- [32] C. -Z. Xu et al. *Phys. Rev. Lett.* **118**, 146402 (2017).
- [33] Y. Onose et al., *Science* **329**, 297 (2010).
- [34] M. Hirschberger, R. Chisnell, Y. S. Lee, and N. P. Ong, *Phys. Rev. Lett.* **115**, 106603 (2015).
- [35] T. Ideue et al., *Phys. Rev. B* **85**, 134411 (2012).
- [36] H. Katsura, N. Nagaosa, and P. A. Lee, *Phys. Rev. Lett.* **104**, 066403 (2010).
- [37] R. Matsumoto and S. Murakami, *Phys. Rev. Lett.* **106**, 197202 (2011); *Phys. Rev. B* **84**, 184406 (2011).
- [38] R. Matsumoto, R. Shindou, and S. Murakami, *Phys. Rev. B* **89**, 054420 (2014).
- [39] A. Mook, J. Henk, and I. Mertig, *Phys. Rev. B* **90**, 024412 (2014); *Phys. Rev. B* **89**, 134409 (2014).
- [40] S. A. Owerre, *J. Appl. Phys.* **120**, 043903 (2016).
- [41] I. Dzyaloshinsky, *J. Phys. Chem. Solids* **4**, 241 (1958).
- [42] T. Moriya, *Phys. Rev.* **120**, 91 (1960).
- [43] M. Elhajal, B. Canals, and C. Lacroix. *Phys. Rev. B* **66**, 014422 (2002).
- [44] D. Grohol et al., *Nat. Mater.* **4**, 323 (2005).
- [45] A. Scheie et al. *Phys. Rev. B* **93**, 180407 (2016).
- [46] X. G. Zheng et al., *Phys. Rev. Lett.* **95**, 057201 (2005).
- [47] T. -H. Han, J. Singleton, J. A. Schlueter, *Phys. Rev. Lett.* **113**, 227203 (2014).
- [48] R. Okuma et al., *Phys. Rev. B* **95**, 094427 (2017).
- [49] M. - T. Suzuki et al., *Phys. Rev. B* **95**, 094406 (2017).
- [50] T. Holstein and H. Primakoff, *Phys. Rev.* **58**, 1098 (1940).
- [51] T. -H. Han et al., *Phys. Rev. B* **93**, 214416 (2016).
- [52] S. A. Owerre, *Phys. Rev. B* **95**, 014422 (2017).
- [53] P. Laurell and G. A. Fiete, *Phys. Rev. B* **98**, 094419 (2018).
- [54] S. Nakatsuji, N. Kiyohara, and T. Higo, *Nature* **527**, 212 (2015).
- [55] N. Kiyohara, T. Tomita, and S. Nakatsuji, *Phys. Rev. Applied* **5**, 064009 (2016).
- [56] A. K. Nayak et al., *Sci. Adv.* **2** e1501870 (2016).
- [57] H. Yang et al., *New J. Phys.* **19** 015008 (2017).
- [58] K. Kuroda et al. *Nat. Mater.* **16**, 1090 (2017).
- [59] J. Kübler and C. Felser, *Europhys. Lett.* **120**, 47002 (2017).